Research Square

Preprints are preliminary reports that have not undergone peer review.
They should not be considered conclusive, used to inform clinical practice,
or referenced by the media as validated information.

Mixed diffusive/martensitic character of the pressure-induced β←→γ transformation in tin

Robin Fréville

freville.rob@gmail.com

ESRF https://orcid.org/0000-0001-8882-2153

Agnès Dewaele

CEA, DAM, DIF

Charles Pépin

CEA https://orcid.org/0000-0002-9638-3303

Nicolas Bruzy

https://orcid.org/0000-0002-4102-1348

Florent Occelli

Matteo Levantino

ESRF - The European Synchrotron https://orcid.org/0000-0002-1224-4809

Nicolas Guignot

Article

Keywords:

Posted Date: June 11th, 2026

DOI: https://doi.org/10.21203/rs.3.rs-9712402/v1

License: This work is licensed under a Creative Commons Attribution 4.0 International License.
Read Full License

Additional Declarations: There is **NO** Competing Interest.

Mixed diffusive/martensitic character of the pressure-induced $\beta \leftrightarrow \gamma$ transformation in tin

Robin Fréville[1,2,*], Agnès Dewaele[3,4], Charles Pépin[3,4], Nicolas Bruzy[3,4], Florent Occelli[3,4], Matteo Levantino[2], Nicolas Guignot[5]

[1] Karlsruhe Institute of Technology, Institute for Applied Materials, P.O. Box 3640, 76021 Karlsruhe, Germany

[2] European Synchrotron Radiation Facility, 71 Avenue des Martyrs, CS 40220, 38043 Grenoble, France

[3] CEA, DAM, DIF, F-91297 Arpajon, France

[4] Université Paris-Saclay, CEA, Laboratoire Matière en Conditions Extrêmes, 91680 Bruyères-le-Châtel, France

[5] Synchrotron Soleil, BP 48, 91192 Gif-sur-Yvette Cedex, France

[*] Corresponding author: robin.freville@esrf.fr

(Dated: May 19, 2026)

Abstract

Solid-solid phase transformation mechanisms need to be understood to establish suitable kinetic laws. Here, the β-Sn $\leftrightarrow$ γ-Sn phase transformations are investigated at different strain rates at 300 K. On one side, single crystals have been statically compressed and characterized using *in situ* x-ray diffraction. Multiple transformation cycles were performed in diamond anvil cells to measure their conditions and the associated microstructures. $(101)_\beta||(110)_\gamma$ and $[10\bar{1}]_\beta||[1\bar{1}1]_\gamma$ orientation relationships (OR) between β-Sn and γ-Sn are observed in most cases, for both direct and reverse transformations. An atomic martensitic transformation mechanism, associated with self-accommodation, is proposed to account for these OR and variant selection. However, γ-Sn $\rightarrow$ β-Sn reversion also presents massive diffusive transformation microstructural features. On the other side, time-resolved (4 µs scale) dynamic diamond anvil cell experiments have been carried out. They confirm that while β-Sn $\rightarrow$ γ-Sn transformation is martensitic and fast ($P_{\beta\rightarrow\gamma}$=10.9 $\pm$ 0.2, insensitive to strain rate), timescales of β-Sn formation and subsequent recrystallization/growth in this phase can be distinguished for the γ-Sn $\rightarrow$ β-Sn transformation. As a result, measured transition pressure $P_{\gamma\rightarrow\beta}$ varies with strain rate, from 9.4$\pm$0.8 GPa to 6.35$\pm$0.4 GPa. A different kinetic description needs to be used for direct and reverse transitions.

I. INTRODUCTION

The knowledge of the equilibrium phase diagram of the elements involved is a prerequisite for any science under extreme conditions. Now that volumetric compression rates can be varied by several decades, from 10^{-4} s^{-1} to 10^{9} s^{-1}, with time-resolved in situ measurements, kinetic effects in phase transformation conditions and subsequent effects on measured phase diagrams have been disclosed for several systems. The strain rate dependence of phase transitions exhibits significant material-specific variations. Shock compression regimes, characterized by strain rates exceeding 10^{6} s^{-1}, induce substantial shifts in the α-Fe$\rightarrow\epsilon$-Fe transition pressure, with reported increases of tens of GPa [1]. Conversely, intermediate strain rates ranging from 10^{0} to 10^{2} s^{-1}, readily accessible via dynamic diamond anvil cell experiments [2], produce negligible effects on the phase transition pathway in iron [3]. However, this behavior is not universal: materials such as TiO_2 demonstrate considerably greater strain rate sensitivity, exhibiting measurable transition pressure shifts at strain rates as low as

10^0 s^{-1} [4, 5]. Notably, strain rate effects can yield counterintuitive outcomes: in certain systems, i.e. Sb [6], Si [7], and Bi [8], high strain rates suppress intermediate high-pressure phases, fundamentally altering the transition sequence.

Understanding such different kinetic behaviors requires a description of the transformation mechanism from atomic to mesoscale. Two classes of solid-solid phase transformations are described in the literature. Martensitic transformations have a 'military' displacive atomic mechanism that produces a new phase seed with a time scale that can be as low as sub-ns; however, they induce elastic stresses that need to be relaxed, which is a phenomenon at the microstructure scale. Reconstructive transformations, with nucleation and diffusional growth steps, sometimes massive, are thermally activated and slower but produce a microstructure at mechanical equilibrium.

Sn (tin) exhibits a rich polymorphism under high pressure and varying temperatures that has been studied with different techniques and platforms. This makes it an archetypal system to study phase transformations in metals and their mechanisms. Under ambient conditions, it adopts a body-centered tetragonal $I4_1/amd$ (β-Sn) structure (4 atoms/unit cell), similar to the high pressure phases of Si and Ge. Above ∼10.8 GPa, β-Sn transforms to another body-centered tetragonal structure (bct), called γ-Sn (space group: $I4/mmm$, same as In-I, 2 atoms/unit cell), with an initial c/a ratio of ∼0.91 (a_γ=3.694 Å and c_γ=3.370 Å at 10.8 GPa). bco ($Immm$), bcc ($Im-3m$), and hcp ($P63/mmc$) [9, 10] phases have been observed at higher pressures, but the present report focuses on β-Sn ↔ γ-Sn transition.

A volume decrease of ∼ 1.9% [10–12] has been measured for the β-Sn→γ-Sn transformation, and a hysteresis between the direct and reverse transition pressures of 2-3 GPa is observed under both static [12] and dynamic [11] compressions. A possible martensitic (or displacive, in this report we use the two words equivalently) mechanism at the atomic scale has been invented by Katzke et al. [13], based on the early work of Musgrave [14]. It involves atomic shuffles of maximum $\pm 3/8 c_\gamma$, and a compressive transformation strain. As far as we know, it has not been validated experimentally, which can be done by measuring the Orientation Relationship (OR) between parent and daughter phases predicted for this mechanism: $(110)_\beta||(100)_\gamma$ and $[001]_\beta||[001]_\gamma$. Katzke mechanism produces a single *variant* for both direct β-Sn → γ-Sn and reverse γ-Sn → β-Sn transitions. The term variant corresponds to one orientation of a daughter phase, for a fixed orientation of a parent phase [15]. In general, dislocation generation and/or twinning allow releasing the martensitic transfor-

mation strain [16]. The 4 known twinning systems described for β-Sn and γ-Sn, or similar phases, that will be used in this work, are described in the Tab. S1 of the Supplementary Materials [17]; the last column of the table indicates how they are noted in this report.

Here, we study $\beta \leftrightarrow \gamma$ phase transformations in tin by static and dynamic compression in diamond anvil cells (DAC). Static *in situ* measurements of microstructures induced by cycling the transformations in starting single crystals disclose the transition mechanisms involved. Two martensitic mechanisms are observed, but the $\gamma \rightarrow \beta$ transformation also bears diffusive features. $\beta \leftrightarrow \gamma$ transformations, induced by dynamic compression/decompression of multi-grain foils, have also been monitored with time-resolved x-ray diffraction (XRD). Only the reversion pressure exhibits a strain rate effect. The measured microstructural evolution complements the static measurements, evidencing strong recrystallization of β-Sn at the ms time scale, which explains the static observations.

II. RESULTS AND DISCUSSION

A. Microstructures observed in static measurements

The static measurements reported here have been carried out using a powder Sn grain (Run 1) and a laminated Sn foil (Run 2), annealed to approach a single crystal state (Fig. 1). These samples were cyclically compressed in DACs, under hydrostatic conditions, to induce $\beta-\gamma-\beta$ transformations, characterized with XRD; see "Methods". Multi-exposure datasets were collected to measure crystal orientations. Transformation conditions and Equation of State are detailed in section S.B of the Supplementary Materials [17]. They are consistent with previous studies, with a direct transformation at 10.9 $\pm$ 0.2 GPa, and a reversion at 9.4 $\pm$ 0.8 GPa (Tab. S2, Fig. S2).

Crystal orientations measured in Run 1 are represented in Fig. 2 as an evolution sketch (a) and pole figures (b-d). Starting from a dominant β_1 orientation (Fig. 1a), three $(101)_\gamma$ twinned orientations (γ_1, γ_2, γ_3) are formed (Fig. 2b). Two ORs are identified: Katzke OR and a second OR defined by $(101)_\beta||(110)_\gamma$ and $[10\bar{1}]_\beta||[1\bar{1}1]_\gamma$, observed between β_1-γ_1 and β_1-γ_3, respectively, within $\sim$10° (i.e. inside experimental uncertainty for this run; Fig. 2b and c). To our knowledge, the second OR found here does not correspond to any mechanism described in the literature. We call it hereafter TW (This Work) OR. Upon reversion, a new

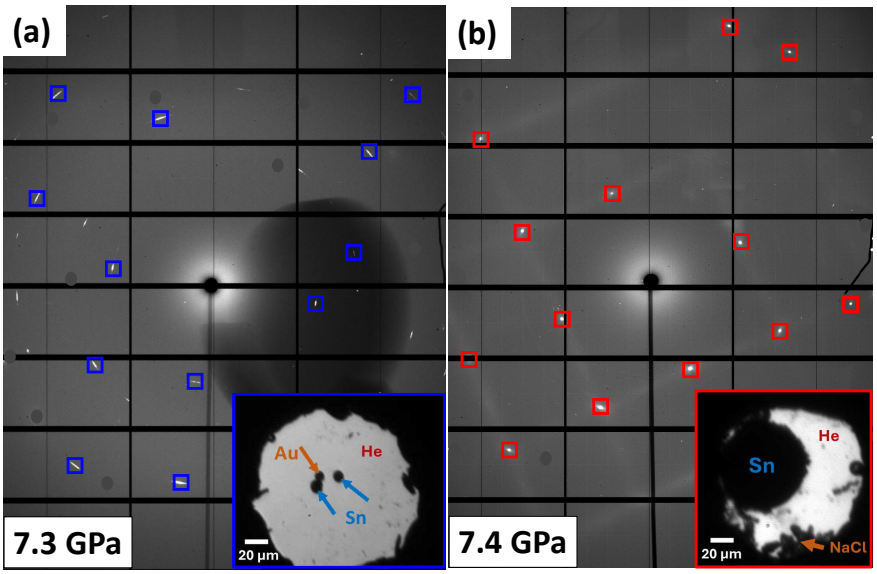


FIG. 1: Diffraction images of starting samples for (a) Run 1 (powder grain) at 7.3 GPa, and (b) Run 2 (annealed foil) at 7.4 GPa. Blue/red square boxes indicate the position of XRD peaks for β_1/β_A single crystals (see text). The insets show pictures of the high pressure chambers.

β-Sn orientation (β_2) forms, with a clear γ_2-β_2 TW OR. It comes to a surprise that three starting γ-Sn orientations produce crystal(s) with one single orientation. This behavior cannot be attributed to a variant selection by memory effect [18], as the new β crystal orientation differs from the starting one. Possible mechanisms include de-twinning in γ-Sn prior to the phase transformation or recrystallization in β-Sn. Two additional $\beta \rightarrow \gamma \rightarrow \beta$ cycles were performed during Run 1: one at 300 K and the other at 425 K. During cycle 2, three γ-Sn orientations (γ_4, γ_5, and γ_6) are produced, all related to β_2 with TW OR (see Fig. S4 of the Supplementary [17]). The reversion restores the crystal back to β_2 orientation. For the last cycle, a sequence: $\beta_2 \rightarrow \gamma_5 \rightarrow \beta_2$ is observed. It is thus similar to cycle 2, except for the variant selection in γ-Sn that could be related to the higher temperature for this cycle (425 K).

In Run 2, one grain β_A, with an XRD signal as presented in Fig. 1b, is present throughout most of the starting sample. Additional grains are observed close to its edges and are not followed. At 11.0 GPa, four γ-Sn orientations (γ_A to γ_D) form, with OR summarized in Fig. 3. TW OR is found three times, the fourth orientation being obtained by subsequent $(101)_\gamma$ twinning. Only one orientation β_B forms during $\gamma \rightarrow \beta$ reversion, from four γ-Sn

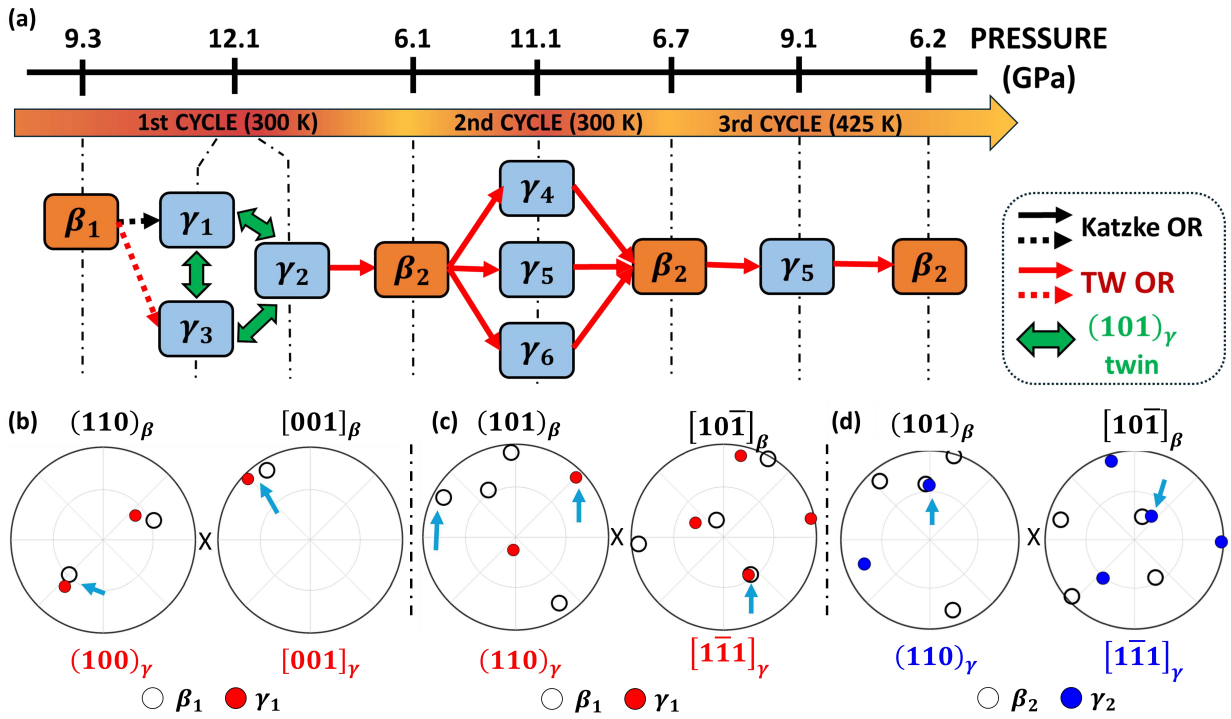


FIG. 2: **Run 1**: (a) Schematic representation of orientations and OR. This work (TW) OR is $(101)_\beta||(110)_\gamma$ and $[10\bar{1}]_\beta||[1\bar{1}1]_\gamma$. Plain/dashed arrows indicate that OR are observed within 2 °/10 ° (see computations in Tab. S6 [17]). (b)-(c) Pole figure showing Katzke OR (b) and TW OR (c) between β_1 (empty black circles) and γ_1 (red dots). In both cases the observed OR present a misorientation of ∼10° compared to the perfect ones. (d) Pole figure showing TW OR between γ_2 (blue dots) and β_2 (empty circles). Blue arrows highlight the coincidences. X (horizontal) is the compression direction.

orientations. Again, de-twinning of γ-Sn could explain this, but the decrease in crystal mosaicity (Supplementary Fig. S3 [17]) suggests crystal healing. Massive mechanisms for solid-solid phase transformation involve nucleation and growth by atomic diffusion steps; they can transform polycrystals into single crystals, as observed here. They are thermally activated and competitive with respect to displacive mechanisms when $T > T_{melt} \times 0.4$ [19]. This is the case here at 9 GPa and 300 K, with an extrapolated melting temperature of β-Sn around 700 K. OR can be reported for massive transformations when the starting nucleus forms with a displacive mechanism, leading to a coherent boundary [19]. Here, an accurate TW OR exists between γ_B and β_B, suggesting that β-Sn nucleates within a γ_B grain and subsequently grows to cover the entire sample.

After Cycle 1, run 2, three additional full $\beta \rightarrow \gamma \rightarrow \beta$ cycles and one compression are performed. Cycle 2 reversion forms a new single crystal (β_C), which is recovered in subsequent cycles. It is interesting to note that β_C orientation has the $\vec{a}$ axis aligned with the direction of compression. The direct transitions produce a more complex microstructure with two main γ-Sn orientations, which become reproducible after the fourth cycle. TW OR is systematically observed, with a $(112)_\gamma$ twinning relationship between two variants (see Fig. 3a-c).

To sum up, β-Sn$\rightarrow\gamma$-Sn$\rightarrow\beta$-Sn transformations exhibit a displacive character as OR are observed between parent and child phases: once, Katzke OR; several times, a new $(101)_\beta||(110)_\gamma$ and $[10\bar{1}]_\beta||[1\bar{1}1]_\gamma$ OR called TW. For the direct $\beta\rightarrow\gamma$ transition, Katzke displacive mechanism — which has only one variant and a uniaxial compressive strain tensor [13] — is coupled with $(101)_\gamma$ twinning, which likely releases transformation stress. In the case of the new mechanism, it seems that the production of two variants diminishes microstructure stress: neither plastic strain nor $(101)_\gamma$ twinning are observed after transformations. Below, we discuss how observed TW OR and variant selection can be interpreted by an atomistic martensitic mechanism. The $\gamma\rightarrow\beta$ transformation exhibits strong reconstructive/massive transformation features (crystal growth and a decrease in mosaicity), even if TW OR is repeatedly observed.

B. $\beta \leftrightarrow \gamma$ martensitic mechanisms

Vigilano software [20] has been used to determine if TW $(101)_\beta||(110)_\gamma$, $[10\bar{1}]_\beta||[1\bar{1}1]_\gamma$ OR corresponds to a new atomistic martensitic mechanism or could result from Katzke mechanism [13] coupled with twinning. All occurrences of TW OR have thus been compared (in terms of misorientation angles) to sequences including Katzke mechanism and up to two twinning steps (listed in Tab. S1 [17]). When double twinning of one phase is involved, the hypothesis is made that the same twinning system is activated at both steps; as recently observed in ϵ-Fe [21] and γ-Fe [18]. The results (tabulated in Tab. S6 [17]) show that Katkze mechanism has to be coupled with at least two twinnings to reproduce the observed OR: $\beta \xrightarrow[(301)\beta]{\text{Twinning}} \beta' \xrightarrow[(301)\beta]{\text{Twinning}} \beta'' \xrightarrow{\text{Katzke}} \gamma$ and $\beta \xrightarrow[(101)\beta]{\text{Twinning}} \beta' \xrightarrow[(101)\beta]{\text{Twinning}} \beta'' \xrightarrow{\text{Katzke}} \gamma$ (or reverse). If the system follows such paths, it is surprising that Katzke OR alone is observed only seldom in our experiments. We thus believe that TW OR are not likely to be explained by Katzke

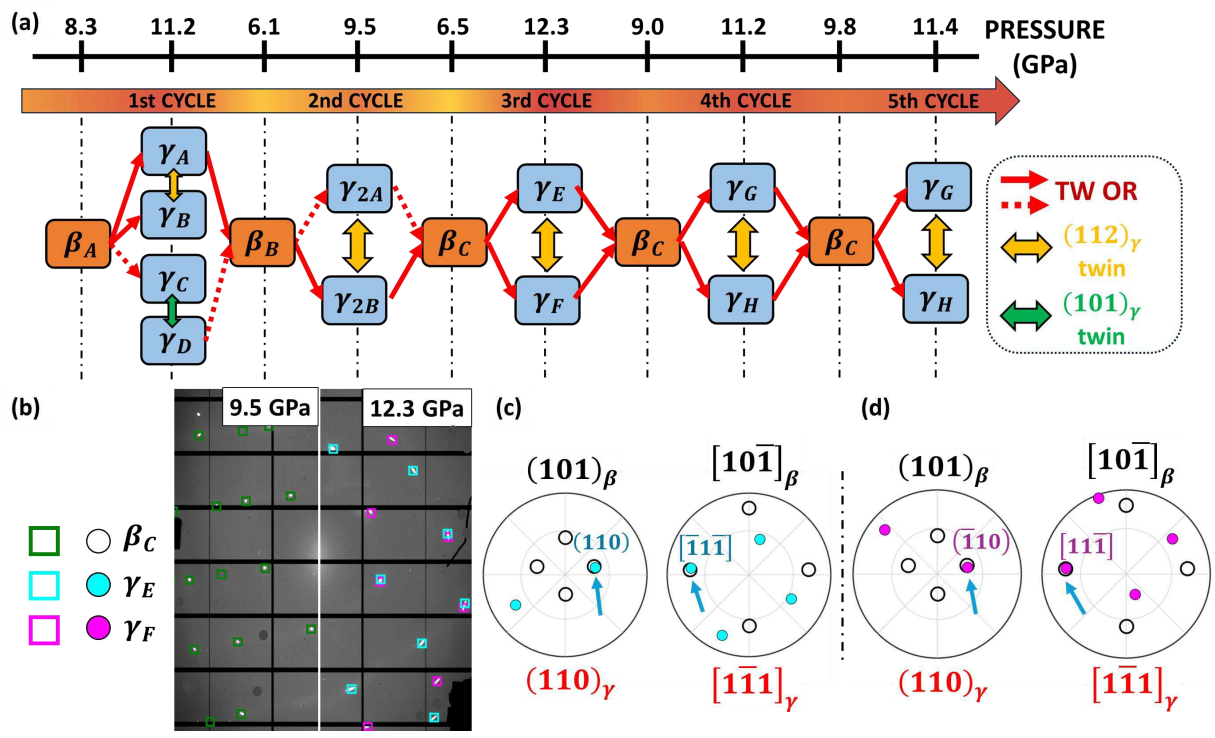


FIG. 3: **Run 2**: (a) Schematic representation of orientations and OR during the experiment. This work (TW) OR is $(101)_\beta||(110)_\gamma$ and $[10\bar{1}]_\beta||[1\bar{1}1]_\gamma$. Plain/dashed arrows indicate that OR are observed within 2 °/10 ° (see computations in the Tab S6 [17]). (b) Composite diffraction images of the β-Sn phase at 9.1 GPa (left) and γ-Sn phase at 12.3 GPa (right). Green, cyan and magenta square boxes indicate the position of XRD peaks for β_C, γ_E and γ_F single crystals during third cycle, respectively. Common diffracted peaks evidence the $(112)_\gamma$ twinning relation between the two variants of the same mechanism (see text). (c)-(d) Pole figures showing TW OR between β_C (empty black circles) and γ_E (cyan dots) and γ_F (magenta dots). In both cases the observed OR present a misorientation of ∼1.5° compared to the perfect ones. Blue arrows highlight the coincidences. The identification of plane and direction related to the mechanism are displayed for γ-Sn. Horizontal line is the compression direction.

mechanism, and consider below an alternative atomistic mechanism.

The atomistic mechanism involved in TW OR is represented in Fig. 4: a $(101)_\beta$ plane must transform into a $(110)_\gamma$ plane; such transformation produces 8 variants, as four equivalent $(101)_\beta$ planes and two different $(110)_\gamma$ planes exist. The transformation requires small atomic shuffles, illustrated in Fig. 4a: a vertical translation of the four atoms located within the

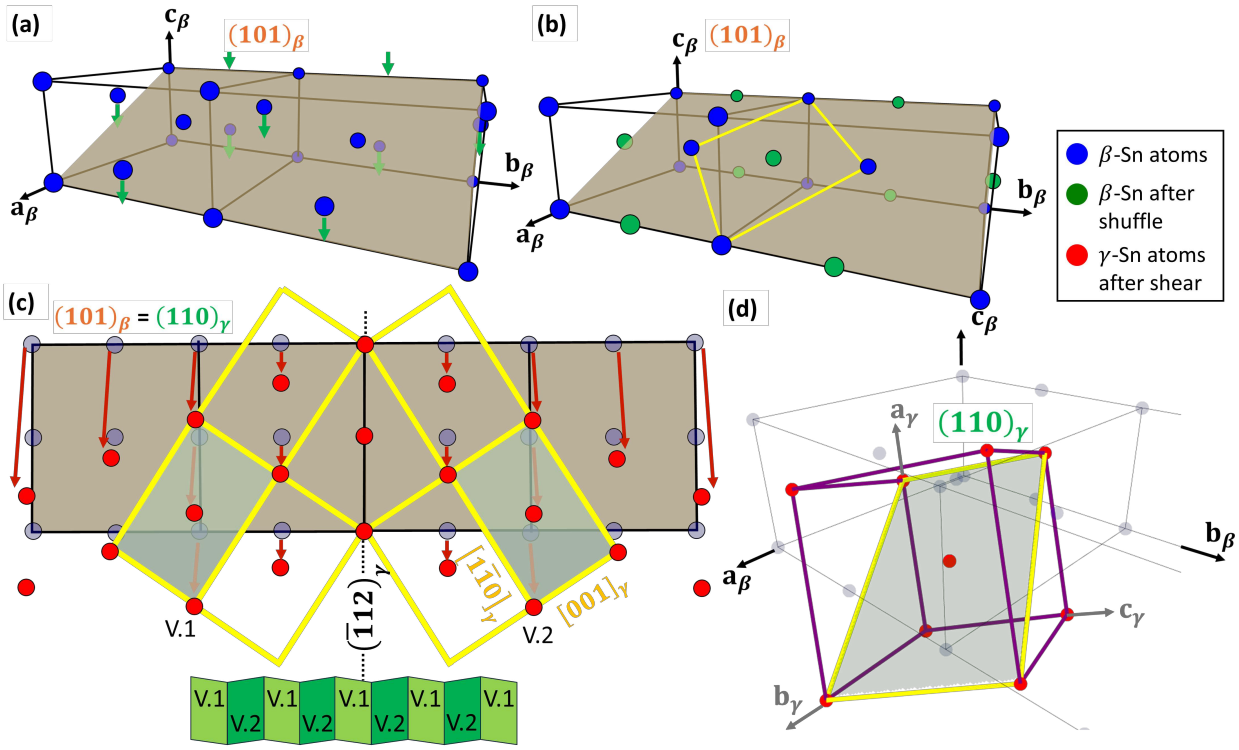


FIG. 4: Schematic illustration of shuffle and shear associated with TW mechanism. **(a)** Shuffle: vertical translation (indicated with green arrows) of four atoms of the conventional unit cell; after shuffle **(b)**, a pattern matching $(110)_\gamma$ planes' configuration appears in $(101)_\beta$ planes (highlighted with yellow lines). Green atoms represent the atoms impacted by shuffle. **(c)** Shear in $(101)_\beta$ plane. Blue/red atoms are the position before/after applying F_1 strain (see section S.H [17]). Two variants V.1 and V.2 can be formed in a symmetric way to reduce the global shear (see text) and form the so-called herringbone microstructure, with $(\bar{1}12)_\gamma$ plane as interface. The yellow rectangle indicates $[1\bar{1}0]_\gamma$ and $[001]_\gamma$ directions. **(d)** Unit cell of γ-Sn (purple rectangular prism with red atoms) represented within β-Sn unit cell.

faces of the conventional dbct unit cell forms the sets of four atoms that outline the future $(110)_\gamma$ pattern. To obtain the required γ-Sn lengths and angles, an additional deformation is required : see Fig. 4c.

The deformation gradient F for this transformation, defined by $F = I + \nabla u$, where I is the identity of second-order tensors and ∇u is the spatial gradient of displacement, is

evaluated in section S.H of the Supplementary Materials [17]. It is:

$$F = \begin{bmatrix} 1.06 & 0.40 & 0.15 \\ 0.25 & 1.02 & 0.47 \\ -0.04 & -0.22 & 0.90 \end{bmatrix} . \quad (1)$$

The norm of the corresponding Green-Lagrange strain tensor $E = \frac{1}{2}\left(F^T F - I\right)$ is 0.64. A zero norm would correspond to an absence of macroscopic strain; 0.64 is a high value, significantly larger than for Katzke mechanism (0.15), that would imply large elastic stresses in the material during the transformation. However, pairs of γ-Sn variants sharing a $(112)_\gamma$ plane are systematically formed (see Figs. 2a and 3a); they correspond to variants V1 and V2 listed in Tab. S5 of the Supplementary Materials [17]. This pairing greatly releases transformation strain: the strain calculated for such pairs of the same size has a magnitude of only 0.104. This is called *self-accommodation* in shape-memory alloys, where the variants of martensite arrange themselves in such a manner that there is no macroscopic change in shape [22]. By similarity with these materials, we can imagine a so-called herringbone microstructure composed of stacked γ-Sn twinned layers sharing (112) interfaces, as schematically illustrated in Fig. 4c. The size of these structures should be smaller than the X-ray beam (8×12 µm), as both orientations are systematically observed on each XRD image. The remaining 0.104 strain mainly consists of shear deformation, that could be facilitated by the low values of the C_{44} and C_{66} stiffness components for both phases. For β-Sn at ambient, C_{44}=22 GPa and C_{66}=24 GPa [23], and ab initio calculations predict that $C_{44} \simeq$11 GPa in γ-Sn [24].

We observe that $\gamma \rightarrow \beta$ transformation exhibits a partially reconstructive character. How this interacts with the displacive mechanism chosen by the system for this transformation is explored below, with the help of time-resolved measurements.

C. Dynamic measurements

In separate experiments, the same $\beta \rightarrow \gamma \rightarrow \beta$ sequences are induced with compression rates varying between 20 and 200 GPa/ms (corresponding to strain rates of ∼400-4000 s^{-1}). Powder samples of Sn are compressed and decompressed in the 1-20 GPa range, without pressure transmitting medium, and characterized with XRD in dynamic-diamond anvil cells (dDAC) at 300 K, see "Methods".

The direct β-Sn$\rightarrow\gamma$-Sn transition proceeds at 11.0 GPa, with no effect of compression rate; this is in line with recent shock measurements where the transition pressure measured at 10^6 GPa/ms compression rate is found to agree with static transition pressure [12, 25]. From the similarity in XRD images, we infer that γ-Sn microstructure consists of powder grains with a size of the same order as starting β-Sn.

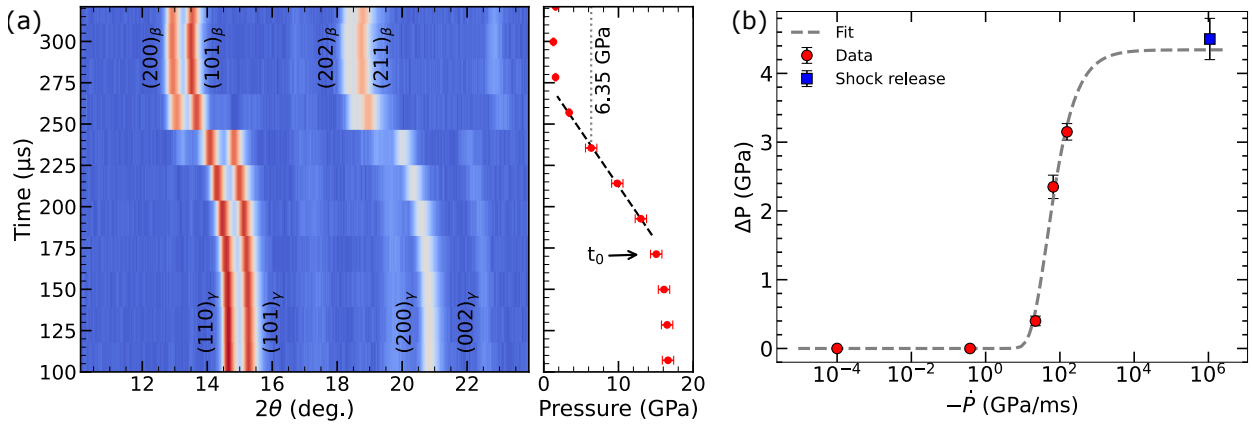


FIG. 5: (a) Representative example of the γ-Sn$\rightarrow\beta$-Sn phase transition measurement with time-resolved XRD under dynamic decompression, starting at t_0. Left: time evolution of the azimuthally integrated XRD signal. The phase transition is observed at t_0+65 μs. Right - pressure vs time. The black dashed line is to a linear fit of decompression pressure, corresponding to a rate of -150 GPa/ms. (b) $\Delta P = P_{static} - P_{dynamic}$, with $P_{static}/P_{dynamic}$ static/dynamic γ-Sn$\rightarrow\beta$-Sn transition pressures *vs.* decompression rate $-\dot{P}$. Our data points alongside the shock release point from Ref. 26 are reported. The gray-dashed lines is the best fit result of Eq. 2, for which the shock release point was not included.

On the contrary, γ-Sn$\rightarrow\beta$-Sn reversion condition exhibits a definite sensitivity to decompression rate. Fig. 5a shows a transition at $P_{dynamic}$=6.35 ± 0.4 GPa for a decompression rate of -150 GPa/ms (to be compared to P_{static}=9.4 ± 0.8 GPa, see Table S2). No γ-Sn$-\beta$-Sn coexistence is observed, the transition being completed between two sequential frames separated by 4 μs. The difference $\Delta P = P_{static} - P_{dynamic}$ measured at various compression rates, including Ref. 26, is plotted in Fig. 5b. It can be fitted with ($\dot{P} < 0$):

$$\Delta P = a \exp(b/\dot{P}) \ , \tag{2}$$

with $a = 4.46$ GPa and $b = 50.5$ GPa/ms. The saturation value a, independently validated by the shock-release data point from Ref. 26, represents the maximum metastability of γ-Sn,

while b describes the transition rate.

The time-resolved XRD measurements also reveal an evolution of β-Sn microstructure at the ms time-scale. γ-Sn$\rightarrow\beta$-Sn transition produces a fine powder of β-Sn, which immediately recrystallizes to form larger single crystalline grains, producing intense XRD peaks on the two-dimensional detector as shown in Fig. 6a.

This evolution has been quantified using the relation between the average single crystal grain size N_g and the number of crystallites N_g contained in the irradiated volume V ($N_g \propto 1/G^3$). The relation can be extended to the number of (hkl) diffraction spots collected on the detector [27, 28]. In particular, we focused here on the high multiplicity $(101)_\beta$ reflection. Diffraction patterns have been azimuthally unrolled, and the number of $(101)_\beta$ diffraction spots (N_{101}) has been measured within 150° azimuthal angle (Fig. 6a bottom); it decreases with time as shown in Fig. 6b. This trend has been fitted with a Burke normal grain growth law [29], relevant for high temperature grain growth kinetics:

$$G^n - G_0^n = kt \ , \tag{3}$$

G_0 is the starting grain size, $n = 2$, and k is the growth constant. The fit result, with $G_0 = 3.06 \pm 0.05$ µm and $k = 1.79 \pm 0.05 \times 10^{-15}$ m^2/µs, is also plotted in Fig. 6b (the uncertainties arise solely from the fitting procedure). This corresponds to an increase in grain size by a factor of 1.7 in 10 ms. Two different timescales are thus revealed by dynamic experiments: nucleation of β-Sn, within less than 4 µs (the time between two successive XRD frames), and its growth by high-temperature recrystallization, with typical timescales of the order of 10 ms.

D. Discussion

The observations made under static and dynamic compression detail our view of β-Sn$\leftrightarrow\gamma$-Sn mechanisms at 300 K. A martensitic mechanism, either coupled with twinning or with a strong variant selection, explains the β-Sn$\rightarrow\gamma$-Sn orientation relations measured in the static experiments. Martensitic transformations are fast, at the ns timescale [25], and our dynamics experiments show that β-Sn$\rightarrow\gamma$-Sn transition conditions are insensitive to compression rate. β-Sn$\rightarrow\gamma$-Sn thus exhibits a strong martensitic character.

On the contrary, dynamic γ-Sn$\rightarrow\beta$-Sn reversion conditions are sensitive to decompression

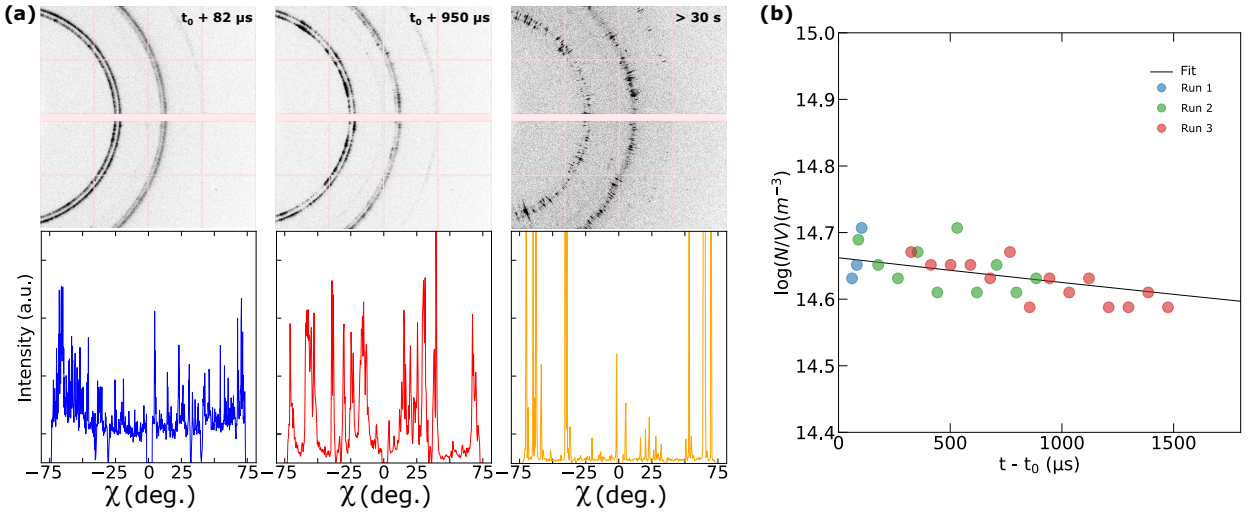


FIG. 6: (a): XRD signal of β-Sn at ∼1.5 GPa, after decompression at -150 GPa/ms. The time indicated in raw XRD images (top) is the delay between the onset of decompression (t_0) and XRD collection. (bottom) One-dimensional patterns obtained by azimuthal projection of the intensity along the $(101)_\beta$ diffraction peak of the two-dimensional patterns. For the runs presented here, γ-Sn→β-Sn transformation is observed at $\sim t_0 + 65$ µs. The number of peaks in bottom graphs corresponds to the number of peaks detected. (b): Time evolution of the volume normalized number of grains N/V in β-Sn detected by XRD after phase transformation in the three different runs. The black line corresponds to a fit with Burke normal grain growth (see text).

rate. Extrapolation of the current measurements to very high decompression rates suggests that γ-Sn could be metastably preserved down to 4.9 GPa, while the static reversion pressure is 9.4 ± 0.8 GPa (ΔP = 4.5 GPa at maximum). Numerous β-Sn grains nucleate as small crystallites in less than a few µs, as shown by the continuous β-Sn XRD rings collected in dynamic experiments. This event is followed by β-Sn single crystal growth within a 10 ms timescale. This is in line with static decompression observations, where similar nucleation and growth steps are inferred for the γ-Sn→β-Sn transition. Due to the smaller number of grains in the statically loaded samples and the proximity to the thermodynamic transition pressure, only a limited number of β-Sn grains are expected to form. They would massively grow at the 10 ms timescale, forming a few healed single crystals. This explains the static formation of a few good quality β-Sn single crystals and the scattered values of transition pressure (9.4 ± 0.8 GPa), the transition being triggered by the formation of one

β-Sn nucleus. Nevertheless, the orientation relations repeatedly observed for the static reversion show that the nucleus is formed with a martensitic mechanism. A pure martensitic kinetics is thus expected at high decompression rate (above $\sim 2\times10^4$ s^{-1}), too fast to allow the growth step, with an hysteresis of 6.1 GPa. In general, γ-Sn$\rightarrow\beta$-Sn reversion is described by a mixed diffusive/martensitic mechanism; its kinetic description requires taking into account this mixed character. Equation 2 could be interpreted as the $n = 1$ case of the Johnson-Mehl-Avrami-Kolmogorov kinetics model [30–32], that describes multiple martensitic nucleation events followed by a massive interface-controlled growth. Grain coarsening by recrystallization is likely to be promoted by residual stresses within the microstructure, which also advocates for a martensitic nucleation process.

III. CONCLUSION

In this work, we investigated the β-Sn $\leftrightarrow$ γ-Sn transformations under pure hydrostatic compression at 300 K and analyzed the microstructures formed over multiple compression–decompression cycles. The effect of strain rate has also been studied in separate experiments. Different mechanisms are disclosed for β-Sn $\rightarrow$ γ-Sn and γ-Sn $\rightarrow$ β-Sn transitions, that should be described with different kinetic laws.

The $\beta \rightarrow \gamma$ transformation is found to be martensitic. During the first transition, (101)[10-1] twinning in γ-Sn is activated, which appears to be a facilitating mechanism. For further transformation cycles, a specific OR, characterized by $(101)_\beta||(110)_\gamma$ and $[10\bar{1}]_\beta||[1\bar{1}1]_\gamma$, is consistently observed with the formation of two specific self-accommodating variants in γ-Sn, and the microstructure stabilizes. We propose that the transformation leads to the formation and accumulation of low-energy, highly compatible interfaces between selected variants at the µm scale. These interfaces are likely reversible at low energetic cost. No strain rate effect on the transition pressure could be measured in the scanned range ($P_{\beta\rightarrow\gamma}$=10.9 $\pm$ 0.2 GPa from 10^{-2} to 4000 s^{-1}).

The $\gamma \rightarrow \beta$ reverse transition presents a massive character allowed by $T/T_{\text{Melting}} \sim 0.4$. Martensitic grain nucleation (attested by static $(101)_\beta||(110)_\gamma$ and $[10\bar{1}]_\beta||[1\bar{1}1]_\gamma$ OR) and subsequent grain growth (with typical time of 10 ms) steps could be distinguished with 4 µs-time-resolved measurements. Increasing the decompression rate to 4000 s^{-1} results in a decrease in the $\gamma \rightarrow \beta$ transition pressure, from 9.4$\pm$0.8 GPa to 6.35$\pm$0.4 GPa. We expect

that γ-Sn cannot be preserved below 4.9 GPa, for higher decompression rates.

Overall, the existence of an asymptotic transition pressure and the pronounced mediation by crystal-modifying processes (twinning, recrystallization, etc.) point toward the necessity of a coupled framework for transformation kinetics, not relying solely on a phenomenological viscosity parameter.

IV. METHODS

Two different types of Sn samples were studied during static experiments: powder grains (99.8% purity, Alfa Aesar) for Run 1 and a 15 µm thickness laminated foil (99.95% purity, Goodfellow), annealed 2h at 450 K under vacuum for Run 2. A disc with a diameter of 80 µm was then cut in the foil with a femtosecond laser. As discussed and presented in Fig. 1, Run 1 powder grains turned out to be β-Sn single crystals, and a large part of Run 2 annealed foil was a β-Sn single crystal.

Samples were loaded in DAC equipped with diamonds with culets of 500/400 µm (Run 1/Run 2) together with a pressure gauge in a pre-indented rhenium gasket (see insets in Fig. 1). Almax-Boehler DAC design was used to ensure a wide angular opening in Run 2. Helium was used as a pressure transmitting medium (PTM) to ensure hydrostatic pressurizing conditions [33, 34]. Pressure was determined using the equation of state (EOS) of Gold [35] or NaCl [36]. Since these EOS parameters were proposed before the publication of the international practical pressure scale (IPPS-Ruby2020 [37]), we modified the Rydberg-Vinet EOS parameters to take into account this new calibration: for Au, $K_0 = 161.9$ GPa, $K_0' = 6.1$ and $V_0 = 67.95$ Å^3/atom; for B1-NaCl, $K_0 = 23.5$ GPa, $K_0' = 5.5$ and $V_0 = 44.90$ Å^3/atom [38].

Experiments were carried out at the PSICHE beamline of SOLEIL synchrotron (France). Angular dispersive X-ray diffraction (XRD) data were collected on a CdTe 2M PILATUS detector, using a monochromatic (0.3738 Å) X-ray beam with a 8×12 µm^2 full width at half maximum (FWHM) spot on the sample. The sample to detector distance, calibrated using a reference CeO_2 sample, was around 370 mm.

The DAC was rotated between $-\theta_{max}$ and $+\theta_{max}$ around a vertical axis and one XRD pattern was collected within θ_{step} (see details in Tab.S4, Fig. S5). In total, $2\theta_{max}/\theta_{step}$ XRD spectra were recorded for these multiexposure datasets. In Run 2, XRD mapping was also

performed throughout the sample using a 50×50 μm^2 grid (25 points) to check homogeneity of its microstructure at selected pressure steps.

The bidimensional images were integrated using Dioptas software [39] to identify phases. Then multiexposure XRD data were processed in order to determine the crystalline orientation of the grains in the sample. TIMELeSS multigrain tools, available from the FABLE project[1] are dedicated to this purpose for DAC experiments. For indexation, Grainspotter [40] was used, as in several studies in the literature [18, 41, 42]. The different grain orientations were exported as Euler angles with a Bunge convention [43]. All Euler angles obtained during this work are available in the Supplementary [17] (Tab. S3). Lattice planes and directions are plotted in pole figures (as presented in several figures in this report) using MTEX toolbox [44] to determine possible OR between phases.

Dynamic compression experiments were performed using a modification of a membrane-DAC [45] with a piston guided by four rods, in conjunction with the Piezosystem Jena HPST 1000/35-25/80 VS45 to apply the force on the piston. A waveform Tabor Electronics WW2074 and an Amplifier Piezosystem Jena RCV 1000/7 are used to deliver the current in the piezoactuator with a chosen profile. This system was synchronized with XRD on ID09 beamlime at ESRF, where a 19 keV quasi-monochromatic beam (spot size ∼25 μm FWHM) was used ($\Delta E/E = 2\%$ [46]). A JUNGFRAU 1M detector was used to collect the XRD signal, operating at up to 250 kHz frame rates, with typical 10 μs exposure times. The set-up for piezo-electric actuator dDAC assemblies was as described in Ref. [47]. The fine control of pre-pressurization allows producing both compression and decompression ramps in the typical range 2-50 GPa, 20-200 GPa/ms, with highly reproducible P vs t paths. The same driving signal was applied to the piezoelectric actuator in successive runs while probing the sample at distinct times, monitoring the β-Sn↔γ-Sn transformations at various compression/decompression rates.

DACs were equipped with Almax-Boehler design DAC with 300 μm culets. Stainless steel gaskets were used for all experiments, indented to 40 μm thickness with a 100 μm-diameter hole for the experimental chamber. Sn powder samples with typical grain sizes of a few microns were loaded without pressure transmitting medium. Pressure was determined using Sn azimuthally integrated XRD signal and EOS of β-Sn and γ-Sn from Ref. [10].

[1] https://github.com/FABLE-3DXRD/TIMEleSS

AUTHORCONTRIBUTIONS

A. D. proposed the research. R. F., A. D., N. B. and N. G. conducted the static experiment. C. P., F. O. and M. L. conducted the dynamic experiment. R. F. and C. P. processed and analysed the data. N. B. performed the Vigilano computations. All authors discussed the interpretation of results and reviewed the manuscript.

DECLARATION OF COMPETING INTEREST

The authors declare that they have no known competing financial interests or personal relationships that could have appeared to influence the work reported in this paper.

DATA AVAILABILITY

Data available on reasonable request from the corresponding author. The raw data for the dynamic experiment can be found at `doi.org/10.15151/ESRF-ES-1126485618`

ACKNOWLEDGMENTS

The authors would like to thank Christophe Denoual for fruitful discussions on the transformation mechanism. We thank Paul Chauvigné and Laura Henry for their help with the experiments. The static experiments have been performed at Soleil during proposals 20221716 and 20240361 (BAG handled by Y. LeGodec). The authors acknowledge the European Synchrotron Radiation Facility for provision of synchrotron radiation facilities on beamline ID09 for the dynamic experiments, during beam time HC-5293.

---

[1] R. F. Smith, J. H. Eggert, D. C. Swift, J. Wang, T. S. Duffy, D. G. Braun, R. E. Rudd, D. B. Reisman, J-P Davis, M. D. Knudson, and G. W. Collins. Time-dependence of the alpha to epsilon phase transformation in iron. *J. Appl. Phys.*, 114(22), DEC 14 2013.

[2] Zs. Jenei, H. P. Liermann, R. Husband, A. S. J. Méndez, D. Pennicard, H. Marquardt, E. F. O'Bannon, A. Pakhomova, Z. Konopkova, K. Glazyrin, M. Wendt, S. Wenz, E. E. McBride,

W. Morgenroth, B. Winkler, A. Rothkirch, M. Hanfland, and W. J. Evans. New dynamic diamond anvil cells for tera-pascal per second fast compression x-ray diffraction experiments. *Review of Scientific Instruments*, 90(6):065114, 06 2019.

[3] Minxue Tang, Rachel Husband, Zuzana Konôpková, Karen Appel, Erik Brambrink, Khachiwan Buakor, Victorien Bouffetier, Jolanta Sztuk-Dambietz, Heinz Graafsma, Torsten Laurus, Hauke Höppner, Alexander Pelka, Sheng-Nian Luo, and Cornelius Strohm. In situ x-ray diffraction of the $\alpha-\varepsilon$ phase transition in iron at intermediate strain rates. *Phys. Rev. Res.*, 8:013135, Feb 2026.

[4] XiaoHui Chen, Yi Zhang, Lei Liu, Shijia Ye, Shourui Li, Qiumin Jing, Junjie Gao, Jun Li, Qiang Wu, Hao Wang, and Chuanlong Lin. Kinetic control of high pressure phase transitions in anatase tio_2. *Phys. Rev. B*, 111:104108, Mar 2025.

[5] I. K. Ocampo, R. F. Smith, D. Kim, V. Prakapenka, S. Speziale, M. Schoelmerich, K. Appel, D. N. Polsin, M. Marshall, S. J. Tracy, F. Miozzi, H. J. Lee, E. Galtier, E. Cunningham, C. McGuire, C. Vennari, A. E. Gleason, and T. S. Duffy. Ultrafast x-ray diffraction of high-pressure phases in dynamically compressed tio_2. *Phys. Rev. B*, 112:104103, Sep 2025.

[6] R. Briggs, M. G. Gorman, A. L. Coleman, R. S. McWilliams, E. E. McBride, D. McGonegle, J. S. Wark, L. Peacock, S. Rothman, S. G. Macleod, C. A. Bolme, A. E. Gleason, G. W. Collins, J. H. Eggert, D. E. Fratanduono, R. F. Smith, E. Galtier, E. Granados, H. J. Lee, B. Nagler, I. Nam, Z. Xing, and M. I. McMahon. Ultrafast x-ray diffraction studies of the phase transitions and equation of state of scandium shock compressed to 82 gpa. *Phys. Rev. Lett.*, 118:025501, Jan 2017.

[7] Emma E. McBride, A. Krygier, A. Ehnes, E. Galtier, M. Harmand, Z. Konôpková, H. J. Lee, H.-P. Liermann, B. Nagler, A. Pelka, M. Rödel, A. Schropp, R. F. Smith, C. Spindloe, D. C. Swift, F. Tavella, S. Toleikis, T. Tschentscher, J. S. Wark, and A. Higginbotham. Phase transition lowering in dynamically compressed silicon. *Nat. Phys.*, 15(1):89–94, 2019.

[8] Charles M. Pépin, Arnaud Sollier, Adrien Marizy, Florent Occelli, Mathias Sander, Raffaella Torchio, and Paul Loubeyre. Kinetics and structural changes in dynamically compressed bismuth. *Phys. Rev. B*, 100:060101, Aug 2019.

[9] Ashkan Salamat, Gaston Garbarino, Agnès Dewaele, Pierre Bouvier, Sylvain Petitgirard, Chris J. Pickard, Paul F. McMillan, and Mohamed Mezouar. Dense close-packed phase of tin above 157 GPa observed experimentally via angle-dispersive X-ray diffraction. *Phys. Rev.*

B, 84:140104, Oct 2011.

[10] Ashkan Salamat, Richard Briggs, Pierre Bouvier, Sylvain Petitgirard, Agnès Dewaele, Melissa E. Cutler, Furio Corà, Dominik Daisenberger, Gaston Garbarino, and Paul F. McMillan. High-pressure structural transformations of Sn up to 138 GPa: Angle-dispersive synchrotron x-ray diffraction study. *Phys. Rev. B*, 88:104104, Sep 2013.

[11] R. Briggs, R. Torchio, A. Sollier, F. Occelli, L. Videau, N. Kretzschmar, and M. Wulff. Observation of the shock-induced β-Sn to b.c.t.-Sn transition using time-resolved X-ray diffraction. *Journal of Synchrotron Radiation*, 26(1):96–101, Jan 2019.

[12] Robin Fréville, Agnès Dewaele, Nicolas Guignot, Philippe Faure, Laura Henry, Gaston Garbarino, and Mohamed Mezouar. High-pressure–high-temperature phase diagram of tin. *Phys. Rev. B*, 109:104116, Mar 2024.

[13] Hannelore Katzke, Ulrich Bismayer, and Pierre Tolédano. Theory of the high-pressure structural phase transitions in Si, Ge, Sn, and Pb. *Phys. Rev. B*, 73:134105, Apr 2006.

[14] MJP Musgrave. On the transition from white tin (β-sn) to the body-centred cubic form under pressure. *Journal of Physics and Chemistry of Solids*, 24(4):557–558, 1963.

[15] Zenji Nishiyama. *Martensitic transformation*. Elsevier, 2012.

[16] J.W. Christian and S. Mahajan. Deformation twinning. *Progress in Materials Science*, 39(1-2):1–157, 1995.

[17] See supplemental material at [url will be inserted by publisher] that includes: (i) notation for twinning elements; (ii) precise conditions of the transformation and EoS; (iii) the crystal quality evolution with cycles; (iv) table of Euler angles determined in this work; (v) a schematic of the diffraction setup; and details about the mechanism: (vi) variants created; (vii) comparison using Vigilano software; and (viii) appendix for computation of the transformation strain. Contains Refs. [10, 12, 16, 35, 36, 48–51].

[18] Robin Fréville, Agnès Dewaele, Nicolas Bruzy, Volodymyr Svitlyk, and Gaston Garbarino. Comparison between mechanisms and microstructures of $\alpha-\gamma, \gamma-\epsilon$, and $\alpha-\epsilon-\alpha$ phase transitions in iron. *Phys. Rev. B*, 107:104105, Mar 2023.

[19] H.I. Aaronson. Mechanisms of the Massive Transformation. *Metall. Mat. Trans. A*, 33A:2285, 2002.

[20] Nicolas Bruzy, Ludovic Druette, Clément Médrala, Étienne Barraud, and Christophe Denoual. Identification of diffusionless transformation sequences from crystal orientation data. *Materials*

Today Communications, 46:112641, 2025.

[21] James A. Hawreliak and Stefan J. Turneaure. Observations of twinning microstructure in iron ramp-compressed through the $\alpha - \epsilon$ phase transition. *Phys. Rev. B*, 106:174306, Nov 2022.

[22] Kaushik Bhattacharya. *Microstructure of martensite: why it forms and how it gives rise to the shape-memory effect*, volume 2. Oxford University Press, 2003.

[23] J. A. Rayne and B. S. Chandrasekhar. Elastic Constants of β Tin from 4.2°K to 300°K. *Phys. Rev.*, 120:1658–1663, Dec 1960.

[24] Mashroor S. Nitol, Khanh Dang, Saryu J. Fensin, Michael I. Baskes, Doyl E. Dickel, and Christopher D. Barrett. Hybrid interatomic potential for Sn. *Phys. Rev. Mater.*, 7:043601, Apr 2023.

[25] Jasper G Threadingham, Xuefei Liang, Edward Leggett, Liam C Smith, Jeremy CF Millett, Glenn Whiteman, Viviane Peçanha-Antonio, Andrew T Boothroyd, David J Chapman, and Daniel E Eakins. Effects of crystal orientation on the shock properties of single crystal tin. *Journal of Applied Physics*, 139(6), 2026.

[26] A. Sollier, C. M. Pépin, M. A. Kozhaev, C. Mariette, W. Reichenbach, and M. Levantino. Development of a laser-driven shock compression platform for time-resolved xrd experiments at the id09 beamline of the european synchrotron radiation facility. *High Pressure Research*, 44(3):418–441, 2024.

[27] T Kubo, T Kondo, A Shimojuku, T Kuwabara, T Kato, T Kikegawa, N Hirao, and Y Ohishi. Time-resolved two-dimensional x-ray diffraction measurements of kinetic properties in polycrystalline high-pressure ices. *Journal of Physics: Conference Series*, 215(1):012022, mar 2010.

[28] Daisuke Yamazaki, Noriyoshi Tsujino, Akira Yoneda, Eiji Ito, Takashi Yoshino, Yoshinori Tange, and Yuji Higo. Grain growth of ϵ-iron: Implications to grain size and its evolution in the earth's inner core. *Earth and Planetary Science Letters*, 459:238–243, 2017.

[29] JE Burke. The fundamentals of recrystallization and grain growth. *Grain Control in Industrial Metallurgy*, pages 1–73, 1949.

[30] W. A. Johnson and R. F. Mehl. Reaction kinetics in processes of nucleation and growth. *Transactions of the American Institute of Mining and Metallurgical Engineers*, 135:416–442, 1939.

[31] M. Avrami. Kinetics of phase change. i. general theory. *Journal of Chemical Physics*, 7:1103–1112, 1939.

[32] A. N. Kolmogorov. On the statistical theory of the crystallization of metals. *Bulletin of the Academy of Sciences of the USSR, Mathematics Series*, 1:355–359, 1937.

[33] Agnès Dewaele and Paul Loubeyre. Pressurizing conditions in helium-pressure-transmitting medium. *High Pressure Research*, 27(4):419–429, 2007.

[34] S Klotz, J-C Chervin, P Munsch, and G Le Marchand. Hydrostatic limits of 11 pressure transmitting media. *Journal of Physics D: Applied Physics*, 42(7):075413–, 2009.

[35] K. Takemura and A. Dewaele. Isothermal equation of state for gold with a He-pressure medium. *Phys. Rev. B*, 78(10):104119–, September 2008.

[36] Agnès Dewaele. Equations of State of Simple Solids (Including Pb, NaCl and LiF) Compressed in Helium or Neon in the Mbar Range. *Minerals*, 9(11), 2019.

[37] Guoyin Shen, Yanbin Wang, Agnes Dewaele, Christine Wu, Dayne E. Fratanduono, Jon Eggert, Stefan Klotz, Kamil F. Dziubek, Paul Loubeyre, Oleg V. Fat'yanov, Paul D. Asimow, Tsutomu Mashimo, Renata M. M. Wentzcovitch, and other members of the IPPS task group. Toward an international practical pressure scale: A proposal for an IPPS ruby gauge (IPPS-Ruby2020). *High Pressure Research*, 40(3):299–314, 2020.

[38] Robin Fréville. *Transitions de phase et microstructures induites dans les métaux en conditions extrêmes : fer et étain*. Theses, Université Paris-Saclay, October 2023.

[39] C. Prescher and V. B. Prakapenka. DIOPTAS: a program for reduction of two-dimensional X-ray diffraction data and data exploration. *High Press. Res.*, 35:223–230, 2015.

[40] Søren Schmidt. *GrainSpotter*: a fast and robust polycrystalline indexing algorithm. *Journal of Applied Crystallography*, 47(1):276–284, Feb 2014.

[41] Angelika Dorothea Rosa, Nadege Hilairet, Sujoy Ghosh, Gaston Garbarino, Jeroen Jacobs, Jean-Philippe Perrillat, Gavin Vaughan, and Sebastien Merkel. In situ monitoring of phase transformation microstructures at Earth's mantle pressure and temperature using multi-grain XRD. *Journal of Applied Crystallography*, 48(5):1346–1354, 2015.

[42] Christopher Langrand, Nadege Hilairet, Carole Nisr, Mathieu Roskosz, Gabor Ribarik, Gavin B. M. Vaughan, and Sebastien Merkel. Reliability of multigrain indexing for orthorhombic polycrystals above 1 Mbar: application to MgSiO3 post-perovskite. *Journal of Applied Crystallography*, 50(1):120–130, 2017.

[43] H.-J. Bunge. Texture analysis in materials science. In H.-J. Bunge, editor, *Texture Analysis in Materials Science*, pages 3–41. Butterworth-Heinemann, 1982.

[44] Florian Bachmann, Ralf Hielscher, and Helmut Schaeben. Grain detection from 2D and 3D EBSD data-specification of the MTEX algorithm. *Ultramicroscopy*, 111(12):1720–1733, 2011.

[45] R. Letoullec, J. P. Pinceaux, and P. Loubeyre. The membrane diamond anvil cell: A new device for generating continuous pressure and temperature variations. *High Pressure Research*, 1(1):77–90, 1988.

[46] Matteo Levantino, Qingyu Kong, Marco Cammarata, Dmitry Khakhulin, Friedrich Schotte, Philip Anfinrud, Victoria Kabanova, Hyotcherl Ihee, Anton Plech, Savo Bratos, and Michael Wulff. Structural dynamics probed by X-ray pulses from synchrotrons and XFELs. *Comptes Rendus. Physique*, 22(S2):75–94, 2021.

[47] Charles M. Pépin, Ramesh André, Florent Occelli, Florian Dembele, Aldo Mozzanica, Viktoria Hinger, Matteo Levantino, and Paul Loubeyre. Metastable water at several compression rates and its freezing kinetics into ice vii. *Nature Communications*, 15(1):8239, 2024.

[48] L. P. Lehman, Y. Xing, T. R. Bieler, and E. J. Cotts. Cyclic twin nucleation in tin-based solder alloys. *Acta Materialia*, 58(10):3546–3556, JUN 2010.

[49] K.N. Tu and D. Turnbull. Direct observation of twinning in lamellae. *Acta Metallurgica*, 18(8):915–&, 1970.

[50] Christina Boukouvala, Elizabeth R. Hopper, Dawn M. Kelly, Philippa J. Knight, John S. Biggins, and Emilie Ringe. Beyond Simple Crystal Systems: Identifying Twinning in Body-Centered Tetragonal Nanoparticles. *Crystal Growth & Design*, 22(1):653–660, 2022.

[51] T. Liu, L. Liang, D. Raabe, and L. Dai. The martensitic transition pathway in steel. *Journal of Materials Science and Technology*, 134:244–253, 2023.

[52] Ludovic Druette, Nicolas Bruzy, and Rémi Lemaire. Vigilano. `https://gitlab.com/vigilano/vigilano.git`, 2025.

Supplementary Files

This is a list of supplementary files associated with this preprint. Click to download.

- Supplementarymechanismtin.pdf
- SupplementarySn.pdf